



A lysosomes and mitochondria dual-targeting AIE-active NIR photosensitizer: Constructing amphiphilic structure for enhanced antitumor activity and two-photon imaging



Shaozhen Wang^a, Yunhui Liao^a, Zhaoji Wu^a, Yihong Peng^a, Yuchen Liu^a, Yinghua Chen^b, Longquan Shao^{c,**}, Zhijie Zeng^{a,***}, Yanshan Liu^{a,*}

^a NMPA Key Laboratory for Research and Evaluation of Drug Metabolism & Guangdong Provincial Key Laboratory of New Drug Screening, School of Pharmaceutical Sciences, Southern Medical University, Guangzhou, 510515, China

^b Guangdong Provincial Key Laboratory of Construction and Detection in Tissue Engineering Department of Histology and Embryology, School of Basic Medical Sciences, Southern Medical University, Guangzhou, 510515, China

^c Stomatological Hospital, Southern Medical University, Guangzhou, 510280, China

ARTICLE INFO

Keywords:

Photosensitizer
Aggregation-induced emission
Dual-organelles targeting
Near-infrared
Photodynamic therapy

ABSTRACT

Development of lysosomes and mitochondria dual-targeting photosensitizer with the virtues of near-infrared (NIR) emission, highly efficient reactive oxygen generation, good phototoxicity and biocompatibility is highly desirable in the field of imaging-guided photodynamic therapy (PDT) for cancer. Herein, a new positively charged amphiphilic organic compound (2-(2-(5-(7-(4-(diphenylamino)phenyl)benzo[c][1,2,5]thiadiazol-4-yl)thiophen-2-yl)vinyl)-3-methylbenzo[d]thiazol-3-ium iodide) (**ADB**) based on a D-A- π -A structure is designed and comprehensively investigated. **ADB** demonstrates special lysosomes and mitochondria dual-organelles targeting, bright NIR aggregation-induced emission (AIE) at 736 nm, high singlet oxygen ($^1\text{O}_2$) quantum yield (0.442), as well as good biocompatibility and photostability. In addition, **ADB** can act as a two-photon imaging agent for the elaborate observation of living cells and blood vessel networks of tissues. Upon light irradiation, obvious decrease of mitochondrial membrane potential (MMP), abnormal mitochondria morphology, as well as phagocytotic vesicles and lysosomal disruption in cells are observed, which further induce cell apoptosis and resulting in enhanced antitumor activity for cancer treatment. *In vivo* experiments reveal that **ADB** can inhibit tumor growth efficiently upon light exposure. These findings demonstrate that this dual-organelles targeted **ADB** has great potential for clinical imaging-guided photodynamic therapy, and this work provides a new avenue for the development of multi-organelles targeted photosensitizers for highly efficient cancer treatment.

1. Introduction

Malignant tumor has increasingly become a public problem for human health [1–3]. Photodynamic therapy, emerging as an enthusiastic method for cancer treatment, has attracted intensive research interest owing to the merits of noninvasiveness, high spatiotemporal selectivity, minimal drug resistance, negligible adverse effect and easy combination with other therapeutics, as comparing with the conventional strategies such as surgery, chemotherapy and radiotherapy [3–8]. Photosensitizers play a critical role in transferring light energy to molecular oxygen to generate reactive oxygen species (such as $^1\text{O}_2$), which then leading to the

apoptosis, necrosis and autophagy of tumor cells [2–13]. Especially, photosensitizers integrating with fluorescence imaging capability are of great interest for they can realize diagnosis and treatment simultaneously [14–18]. Some traditional photosensitizers, including phthalocyanine, porphyrin or chlorin derivatives, have been developed and applied clinically or preclinically for PDT [2,5,7,18–20]. However, the poor singlet oxygen production efficiency, photobleaching, low photostability, and limited fluorescence emission in aqueous media caused by aggregation-caused quenching (ACQ) effect, have greatly limited their applications [16,19–22].

The discovery of AIE phenomenon in 2001 by Tang provides an

* Corresponding author.

** Corresponding author.

*** Corresponding author.

E-mail addresses: shaolongquan@smu.edu.cn (L. Shao), zzjie@smu.edu.cn (Z. Zeng), liuys9@smu.edu.cn (Y. Liu).

excellent choice for the solution of ACQ problem [23]. AIE fluorophores with twisted conformation and reduced intermolecular π - π stacking exhibit weak luminescence in solutions but bright fluorescence in aggregate states via the mechanism of restriction of intramolecular motion [24,25]. A variety of AIE luminogens have been developed and found huge potential in sensing, bioimaging and disease theranostics [26–33]. Investigations have shown that AIE luminogens not only emit strong fluorescence in aggregate state, but also possessing the virtues of sensitive photosensitizing and high singlet oxygen production [29,30,34–36]. Moreover, elaborately-designed AIE luminogens could exhibit good photostability, excellent biocompatibility and two-photon fluorescence imaging, demonstrating immense potential as photosensitizers for PDT [8,22,28,37–40].

Due to the short lifetime (<40 ns) and small diffusion radius (<20 nm) of ROS [37,41,42], the accumulation of photosensitizers in subcellular organelles is usually necessary to enhance PDT efficiency. Mitochondria, known as the powerhouse of eukaryotic cells, play significant roles in energy supply, biosynthesis, signaling and cell differentiation [8,37,43]. Mitochondria are promising target sites of $^1\text{O}_2$ for its function in regulating cellular redox status. Lysosomes are monolayered digestive compartments responsible for degradation of biomacromolecules, and also play vital roles in mediating fundamental life activities such as intracellular transportation, metabolic adaptation, cell apoptosis and necrosis [8,39,44]. The extracellular nanoparticles are usually captured by lysosomes under the endocytosis pathway [45]. Tang and Yoon et al. have designed a number of D-A structured mitochondria- or lysosomes-targeted photosensitizers and found that they could significantly promote cancer ablation [39,46,47]. However, these photosensitizers could only target single organelle. It is considered that AIE fluorophores which can simultaneously accumulate in mitochondria and lysosomes would greatly enhance the precise cancer therapy [8,48–50]. So far, the dual-organelles targeting AIEgen, as well as its anti-cancer mechanism, has been rarely reported. Therefore, the development of mitochondria and lysosomes dual-organelles targeting photosensitizer is highly desirable for photodynamic therapy.

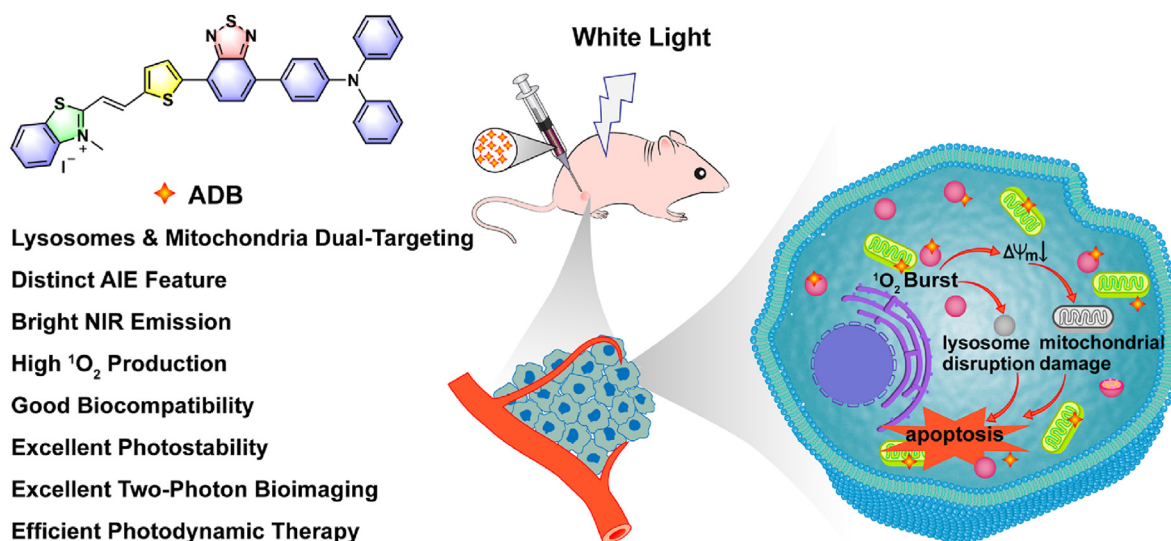
In this study, a new amphiphilic organic NIR photosensitizer **ADB** with a D-A- π -A structure was developed. This cationic AIE fluorophore was rationally designed by adopting triphenylamine as the electron donor and 2,1,3-benzothiadiazole and 2,3-dimethylbenzo[d]thiazol-3-ium iodide groups as combined electron acceptors. **ADB** exhibited bright NIR emission at 736 nm with a Stokes shift of 203 nm, high $^1\text{O}_2$ generation efficiency, as well as good biocompatibility and photostability. In this structure, the lipophilic segment facilitated the insertion of **ADB** into

the mitochondrial membrane, and the electrostatic interaction between **ADB** and mitochondria was enhanced by the cationic part, enabling the mitochondrial targeting of the AIEgen **ADB**. At the same time, lysosomes, known as the “waste disposal station” in the cell, are single membrane-enclosed vesicles composed of a 7–10 nm phospholipid bilayer, the cationic characteristics of **ADB** may facilitate the endocytosis of the nanoparticles into lysosomes, resulting in the formation of phagocytotic vesicles as well as lysosomal disruption, which will then trigger the release of hydrolases into cytoplasm, leading to a series of responses that are associated with cell death [45]. Therefore, in addition to the impressive optical properties, **ADB** exhibited interesting mitochondria and lysosomes dual-organelles targeting capability. *In vitro* and *in vivo* experiments revealed that **ADB** facilitate high quality cell and tissue two-photon bioimaging, and effectively inhibit tumor growth upon white light irradiation (Scheme 1). These studies demonstrated that **ADB** would become a potential photosensitizer for clinical two-photon bioimaging and targeted photodynamic therapy. Furthermore, our work provides new insight for the design and construction of multi-organelles targeting organic photosensitizers for phototheranostics.

2. Experimental section

2.1. Materials

4-(Diphenylamino)phenylboronic acid, 4,7-dibromo-2,1,3-benzothiadiazole, 5-(4,4,5,5-tetramethyl-1,3,2-dioxaborolan-2-yl)thiophene-2-carbaldehyde, 2-methyl-benzo[d]thiazole and tetrakis(triphenylphosphine)palladium ($\text{Pd}(\text{PPh}_3)_4$) were purchased from Bide Pharmatech Ltd. ABDA was obtained from Beijing MREDA Technology Co., Ltd. The widely used commercial photosensitizer RB was supplied by Shanghai Yuanye Bio-Technology Co., Ltd. Fetal bovine serum (FBS) was obtained from Wuhan ProcCell Life Science&Technology Co., Ltd. Dulbecco's modified eagle medium (DMEM), phosphate buffered saline (PBS), penicillin-streptomycin and trypsin-EDTA solution were purchased from Gibco (Thermo Fisher, US). DAPI, Hoechst 33342 and a Live (Calcein-AM)/Dead (propidium iodide, PI) viability/cytotoxicity kit were purchased from Shanghai BioScience Co., Ltd. DCFH-DA, Lyso-Tracker Green, Tunel Apoptosis Assay Kit and JC-1 were purchased from Beyotime. MitoTracker Orange was supplied by Nanjing EnoGene Biotechnology Co., Ltd. Acridine Orange Detection Kit was obtained from Beijing Leagene Biotechnology Co., Ltd. All reagents and solvents were obtained commercially and used without further purification unless otherwise noted.



Scheme 1. Schematic illustration of the chemical structure of **ADB** and its application for lysosomes- and mitochondria-targeted photodynamic cancer therapy.

2.2. Measurements and characterizations

The ^1H NMR and ^{13}C NMR spectra of all compounds were tested on a 400 MHz Brücker spectrometer. HRMS were performed with Waters Xevo G2-XS qtof Mass Spectrometer. The UV-vis spectra were captured by a Metash UV-6000 spectrophotometer. Fluorescence spectra and fluorescence lifetime were detected on a Transient Steady-state Fluorescence Spectrometer (Edinburgh, FLS 980). The absolute fluorescence quantum yield was determined by a hamamatsu absolute PL quantum yield spectrometer C11347. The dynamic light scattering (DLS) size distribution was determined by a Malvern Zetasizer Nano instrument. Transmission electron microscope (TEM) images were recorded by a JEM 2100 microscope. The CLSM images were acquired on Olympus FV3000 and ZEISS Axio Observer A1. The two-photon fluorescence images were collected by a FV1200MPE multi-photon laser scanning microscopy. The mitochondrial morphology was examined under a Hitachi H-7500 transmission electron microscope. *In vivo* imaging and *in vitro* organ fluorescence images were obtained by a PerkinElmer IVIS Lumina II pre-clinical imaging system. Photodynamic experiments were implemented by using a 400–700 nm xenon lamp (PL-X500D, Beijing Precise Technology Co., Ltd.).

2.3. Synthesis of 4-(7-Bromo-2,1,3-benzothiadiazol-4-yl)-N,N-diphenylbenzenamine (compound A1)

The synthetic method of **A1** was similar as we reported previously [28]. In a 100 mL Schlenk tube, 4,7-dibromo-2,1,3-benzothiadiazole (2.92 g, 10 mmol), 4-(diphenylamino)phenylboronic acid (2.89 g, 10 mmol), Pd(PPh₃)₄ (0.46 g, 0.4 mmol) and K₂CO₃ (3.31 g, 24 mmol) were dissolved in THF/water mixture (v/v = 50: 12). The reaction was carried out at 90 °C under the protection of nitrogen for 20 h. After cooling, deionized water was added to quench the reaction, then the mixture was extracted with dichloromethane (3 × 40 mL). The organic layer was dried with anhydrous magnesium sulfate, then the solvent was removed by vacuum evaporation. The crude product was purified by column chromatography (dichloromethane: petroleum = 1: 2), yielding pure **A1** (2.37 g, 52%) as orange powder. ^1H NMR (400 MHz, CD₂Cl₂, δ): 7.91 (d, J = 7.6 Hz, 1H), 7.83 (d, J = 8.6 Hz, 2H), 7.56 (d, J = 7.6 Hz, 1H), 7.31 (d, J = 7.6 Hz, 4H), 7.17 (d, J = 8.0 Hz, 6H), 7.09 (t, J = 7.3 Hz, 2H).

2.4. Synthesis of 5-[7-[4-(Diphenylamino)phenyl]-2,1,3-benzothiadiazol-4-yl]-2-thiophene-carboxaldehyde (compound A2)

Compound **A2** was also prepared via the similar method of **A1** as we reported previously [28]. In a 100 mL Schlenk tube, compound **A1** (1.83 g, 4 mmol), 5-(4,4,5,5-tetramethyl-1,3,2-dioxaborolan-2-yl)thiophene-2-carbaldehyde (1.14 g, 4.8 mmol) and Pd(PPh₃)₄ (0.184 g, 0.16 mmol) were added to a mixture of THF (50 mL) and aqueous solution of K₂CO₃ (2 M, 12 mL). The mixture was stirred at 90 °C under an atmosphere of nitrogen for 20 h. After the mixture was cooled down, it was poured into deionized water to quench the reaction. The mixture was extracted with dichloromethane for three times, then the organic layer was dried over magnesium sulfate and the solvent was removed by vacuum evaporation. The crude sample was purified by column chromatography (dichloromethane: petroleum = 1: 4) to obtain compound **A2** as red powder (1.13 g, 58%). ^1H NMR (400 MHz, CD₂Cl₂, δ): 9.97 (s, 1H), 8.21 (s, 1H), 8.09 (d, J = 7.2 Hz, 1H), 7.93–7.87 (m, 3H), 7.77 (d, J = 7.2 Hz, 1H), 7.32 (t, J = 7.3 Hz, 4H), 7.18 (d, J = 7.6 Hz, 6H), 7.10 (t, J = 6.8 Hz, 2H).

2.5. Synthesis of ADB

2,3-dimethylbenzo[d]thiazol-3-ium iodide (0.35 g, 1.2 mmol) and compound **A2** (0.49 g, 1 mmol) were dissolved in 20 mL of methanol/dichloromethane (v/v = 3: 1) mixed solvent, then 0.5 mmol of pyridine was added. The mixture was stirred at 68 °C for 17 h. After cooling to

room temperature, the solvent was removed by vacuum evaporation and the resulting residue was washed several times with ether and methanol to obtain product **ADB** as black powder. (0.61 g, 80%). ^1H NMR (400 MHz, DMSO-*d*₆, δ): 8.42 (d, J = 15.5 Hz, 1H), 8.34 (dd, J = 16.0, 7.8 Hz, 2H), 8.26 (d, J = 3.7 Hz, 1H), 8.18 (d, J = 8.3 Hz, 1H), 8.05 (d, J = 3.6 Hz, 1H), 7.96 (d, J = 8.4 Hz, 2H), 7.91 (d, J = 7.6 Hz, 1H), 7.80 (t, J = 7.7 Hz, 1H), 7.72–7.68 (m, 2H), 7.38–7.35 (m, 4H), 7.10 (m, 8H), 4.32 (s, 3H). ^{13}C NMR (100 MHz, DMSO-*d*₆, δ): 171.44, 153.44, 152.28, 148.32, 147.17, 146.39, 142.42, 141.26, 141.05, 136.24, 133.38, 130.74, 130.23, 130.04, 129.80, 128.87, 128.68, 128.15, 127.82, 127.60, 125.23, 124.63, 124.32, 123.91, 122.27, 117.07, 112.02, 36.73. HRMS (ESI) m/z : [M]⁺ calcd for C₃₈H₂₇N₄S₃, 635.1392; found, 635.1394.

2.6. Evaluation of $^1\text{O}_2$ generation

In order to detect the $^1\text{O}_2$ generation ability of **ADB**, ABDA was used as an active oxygen detector. **ADB** solution in DMSO (1 mmol, 10 μL) and ABDA solution in DMSO (10 mmol, 14 μL) were added into 1.976 mL of water so that the final concentrations of **ADB** and ABDA were 5 μM and 70 μM , respectively. Then, the mixed solution was irradiated with white light (400–700 nm, 50 mW cm⁻²). RB and ABDA solution in absence of **ADB** were chosen as the control groups. The absorption spectra of the solutions were recorded by UV-vis spectrophotometer.

2.7. Measurement of $^1\text{O}_2$ generation quantum yield

ABDA was used as an active oxygen indicator. Preparing the aqueous solution of RB and **ADB** and adjusting the concentrations so that the absorption maxima of both of them were 0.2 OD. Then the solutions were irradiated with white light (400–700 nm, 50 mW cm⁻²) for 10 min, and the absorbance of ABDA at 378 nm was recorded every 30 s. The $^1\text{O}_2$ generation quantum yield of **ADB** in water was calculated by the following equation [51].

$$\Phi_{\text{ADB}} = \Phi_{\text{RB}} (K_{\text{ADB}} \cdot A_{\text{RB}}) / (K_{\text{RB}} \cdot A_{\text{ADB}})$$

Φ_{RB} is the ROS quantum yield of RB, which is 0.75 in water.

2.8. Cell culture

Cells were cultured in DMEM medium at 37 °C in a 5% CO₂ atmosphere. The DMEM medium was supplemented with 10% FBS and 1% antibiotics (penicillin-streptomycin).

2.9. Cytotoxicity and phototoxicity assessment of ADB

MTT assay was used to detect the biocompatibility and toxicity of **ADB**. The HepG2, HeLa, MCF-7 and MCF-10 A cells were seeded in 96-well plates and cultured for 24 h. Then the medium was replaced by fresh DMEM containing different concentrations of **ADB**. After 24 h, the cells were washed with PBS for three times and co-incubated with MTT working solution for 4 h in the dark. Then the MTT solution was sucked out and the cells were stained with DMSO for 15 min. The absorbance of each well at 490 nm was detected with a microplate reader.

The phototoxicity of **ADB** was also evaluated by MTT assay. MCF-7 cells were incubated with DMEM containing different concentrations of **ADB** for 6 h. Then the cells were irradiated with white light (400–700 nm, 50 mW cm⁻²) for 10 min and cultured in the dark for 18 h, then the absorbance at 490 nm was measured by a microplate reader.

2.10. Confocal images

MCF-7 cells were seeded in 20 mm glass bottom cell culture dishes and cultured 24 h to grow until a confluence of around 80%. Then, the medium was removed and replaced by fresh DMEM containing **ADB** (4, 8, 12, 16, 20 μM). After treating for 6 h, the medium was removed and

the cells were washed three times with PBS. Then cells were imaged by an Olympus FV3000 confocal laser scanning microscope.

2.11. Confocal colocalization experiments

MCF-7 or MCF-10 A cells (5×10^4 cells/well) were inoculated in glass bottom cell culture dishes at 37°C in 5% CO_2 atmosphere for 24 h. After removing the medium, ADB (20 μM) was added to incubate with MCF-7 or MCF-10 A cells for 1, 2, 4 and 8 h, respectively. After washing the cells by PBS, Lyso-Tracker Green (50 nM) and Mito-Tracker Orange (30 nM) were added and incubated for 15 min respectively. Finally, the residual probe was washed off with PBS for three times. Cells were imaged by an Olympus FV3000 confocal laser scanning microscope and the colocalization coefficient was calculated by Image J.

2.12. Two-photon cell and tissue imaging experiments

MCF-7 cells in logarithmic growth stage were seeded in glass bottom cell culture dishes for 24 h. Then the medium was replaced by fresh DMEM containing ADB (20 μM). After incubation for 6 h, the medium was removed and the cells were washed three times with PBS. The fluorescence intensity of the cells under different excitation wavelengths (740–880 nm) were measured by a FV1200MPE multi-photon laser scanning microscopy.

For *In vivo* tissue fluorescence imaging, ADB (3 mg kg^{-1}) was injected into BALB/c nude mice via tail vein. After anesthetizing the mice by 10% pentobarbital, the enterocoelia was opened and the mesenteric vessels were fixed with a small animal organ fixation adsorber. Then the fluorescence imaging of mesenteric vessels was observed with a FV1200MPE multi-photon laser scanning microscopy ($\lambda_{\text{ex}} = 800$ nm).

2.13. Detection of intracellular ROS

MCF-7 cells (5×10^4 cells/well) in the logarithmic growth stage were seeded in glass bottom cell culture dishes for 24 h. Subsequently, ADB (20 μM) was added to the cell dishes and incubated for 6 h. Then the cells were irradiated with white light (400–700 nm, 50 mW cm^{-2}) for 10 min. After washing by PBS for three times, the cells were cocultured with DCFH-DA (10 μM) in the dark for 50 min, then a ZEISS Axio Observer A1 microscope was used to record the intracellular fluorescence.

2.14. Live/dead cell staining assay

MCF-7 cells were incubated with ADB (20 μM) for 6 h. After washing with PBS, the cells were exposed to white light (400–700 nm, 50 mW cm^{-2}) for 10 min. Then the cells were cultured in the dark for 1 h. The medium was sucked out, followed by the addition of fresh DMEM containing Calcein AM and PI. After staining for 15 min, the survival of the cells was observed by an Olympus FV3000 confocal laser scanning microscope.

2.15. Mitochondria membrane potential (MMP) analysis

MCF-7 cells were cultured in the confocal culture dishes at 37°C under an atmosphere containing 5% CO_2 for 24 h. MCF-7 cells were then washed by PBS and incubated with DMEM containing ADB (20 μM) for 6 h. After irradiating with white light (400–700 nm, 50 mW cm^{-2}) for 10 min and then cultured in dark for 1 h, cells were washed with PBS and treated with 1 mL DMEM containing JC-1 probe (10 μM) for 20 min. Finally, the cells were washed with PBS three times and imaged by the FV 3000 confocal laser scanning microscope.

2.16. Mitochondrial damage evidenced by Bio-TEM

MCF-7 cells were incubated with ADB (20 μM) for 6 h. Then the cells were irradiated with white light (400–700 nm, 50 mW cm^{-2}) for 10 min.

1 h later, the cells were washed with PBS and digested by trypsin solution without EDTA, then the cells were fixed with 2.5% glutaraldehyde in PBS buffer. After staining at room temperature for 1 h and incubated overnight at 4°C , glutaraldehyde was removed and the cells were washed with PBS. Sections were postfixed with 2% osmium, rinsed, dehydrated and embedded in durcupan resin. Ultrathin sections were cut with a diamond knife, stained with lead citrate and examined under a Hitachi H-7500 transmission electron microscope.

2.17. Lysosome disruption analysis

MCF-7 cells (5×10^4 cells/well) were seeded in glass bottom cell culture dishes for 24 h. Subsequently, ADB (20 μM) was incubated with cells for 6 h. Then the cells were irradiated with white light (400–700 nm, 50 mW cm^{-2}) for 10 min and cultured in the dark for 1 h. After washing by PBS for three times, the cells were stained with acridine orange (AO) for 15 min. Then an Olympus FV3000 confocal laser scanning microscope was used to observe the intracellular fluorescence (green channel: excited at 488 nm, collected at 500–540 nm; red channel: excited at 561 nm, collected at 570–620 nm).

2.18. Tumor-bearing mouse model

All animals were provided by the Laboratory Animal Center of Southern Medical University with certificates (approval number: No.44002100032650). All animal experiments were carried out according to the procedures approved by the Care and Use of Laboratory Animals of Southern Medical University and strictly conformed to the guidelines formulated by Southern Medical University Experimental Animal Ethics Committee.

MCF-7 tumor-bearing mouse model: MCF-7 cells (2×10^6 cells in 0.1 mL of PBS) were injected subcutaneously into the right flank of the BALB/c nude mice (5 weeks, female) to establish tumor model. When the tumor volume developed to nearly 100 mm^3 , the mice were allowed for *in vivo* imaging and PDT experiments.

2.19. In vivo imaging

When the tumor volume reached about 100 mm^3 , MCF-7 tumor-bearing mouse was intratumorally injected with PBS containing ADB (3 mg kg^{-1}). A multispectral small animal imaging system was used to observe the *in vivo* fluorescence signals at different time after injection (10 min, 1 h, 3 h, 12 h, 24 h, 48 h, 72 h). The excitation wavelength was 465 nm, and the fluorescence was collected at 810 nm. 72 h later, the mouse was sacrificed and the organs (heart, liver, spleen, lung, kidney and tumor) were taken to observe the fluorescence intensity.

2.20. Assessment of in vivo PDT effect

When the tumor volumes reached about 100 mm^3 , 16 mice were randomly divided into four groups ($n = 4$) for different treatments: (1) saline; (2) saline + light; (3) ADB and (4) ADB + light. In Group 1 and 3, the mice were fed in the dark after intratumoral injection of 50 μL saline or ADB (3 mg kg^{-1}), respectively. The mice in Group 2 and 4 were intratumorally injected with 50 μL saline or ADB (3 mg kg^{-1}), respectively, and then the tumor sites of the mice were irradiated with white light (400–700 nm, 100 mW cm^{-2}) for 10 min at day 0, 3, 6, 9. The body weight and tumor volume of the mice in each group were measured and recorded every two days (volume = width² × length/2) to evaluate the *in vivo* PDT effect.

2.21. Hematological and histological examinations

After complete treatment for 14 days, the mice were sacrificed, and the blood, tumors and main organs (heart, liver, spleen, lung and kidney) were collected for analysis. The tumors and organs were immersed in 4%

paraformaldehyde solution for fixation, then dehydrated, paraffin embedded, and sectioned. The sections were stained with hematoxylin & eosin (H&E) for histological examinations, and the tumor sections were also analyzed by TUNEL staining assay. The blood samples were dropped into tubes containing Anticoagulant Sodium Citrate Solution, then the samples were shaken up, and further used for whole blood cell analysis.

2.22. Statistical analysis

The values of the bar charts were expressed as mean \pm standard deviation. Graphic drawing was drawn on Origin 8 software. The statistical significance of differences between groups was performed by using ordinary one-way ANOVA method on the GraphPad Prism 8.0.1 software. A value of $P < 0.05$ was considered significant and were indicated with asterisks: * $P < 0.05$, ** $P < 0.01$, *** $P < 0.001$, **** $P < 0.0001$.

3. Results and discussion

3.1. Design and optical characterization of ADB

Encouraged by the excellent light-harvesting ability and power-conversion efficiency of organic sensitizers based on D-A- π -A structure in solar energy conversion studies [52], the concept of combined acceptor has been introduced into the construction of PDT photosensitizers, which demonstrated obvious potential in improving the absorption and emission of the photosensitizers [6,28]. In this contribution, a rigid molecule, namely ADB (Fig. 1a), based on a D-A- π -A skeleton was designed and synthesized with the expectation to endow it with AIE characteristics, two-photon absorption, long-wavelength absorption and $^1\text{O}_2$ generation upon irradiation. Triphenylamine was chosen as an electron donor, benzothiazole as an auxiliary electron acceptor, and 2,3-dimethylbenzo[d]thiazol-3-ium iodide as a second acceptor, which was very conducive to render the photosensitizer with red-shifted absorption and good water solubility. In addition, a

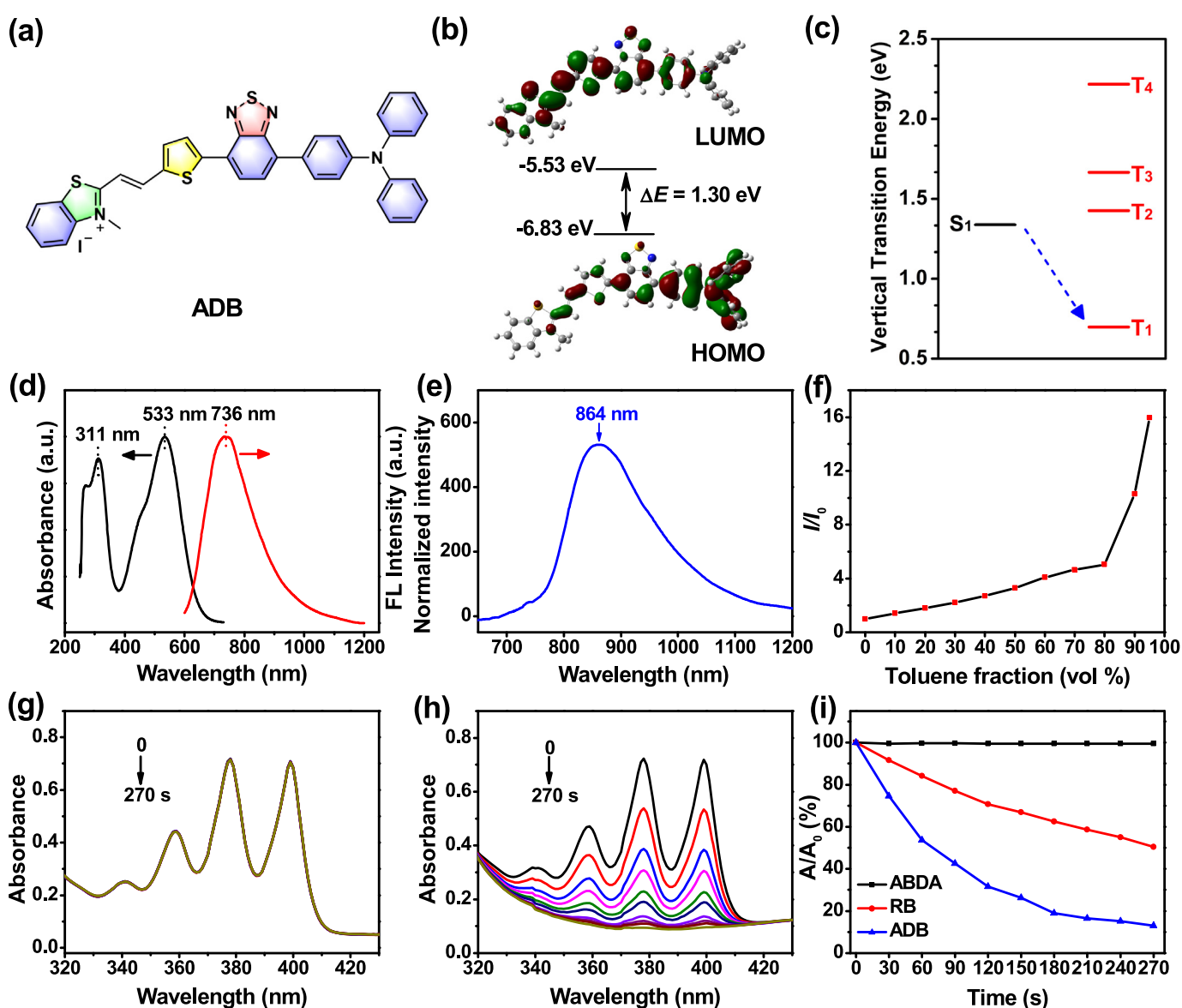


Fig. 1. (a) Chemical structure of ADB. The (b) HOMO and LUMO distributions and (c) ΔE_{ST} value of ADB obtained by DFT/B3LYP/6-31G(d,p) Gaussian calculations. (d) Absorption and emission spectra of ADB in DMSO. (e) Normalized emission spectrum of ADB solid powder. (f) Fluorescence intensity ratios (I/I_0) of ADB in toluene/DMSO mixture with different f_s at the maximum emission wavelength; I_0 is the fluorescence intensity of ADB in DMSO. Degradation of (g) ABDA and (h) ABDA with ADB under light irradiation (400–700 nm, 50 mW cm^{-2}). (i) Decomposition of ABDA under the presence of ADB or RB upon irradiation, where A_0 and A are the absorbance of ABDA at 378 nm before and after irradiation, respectively. [ADB or RB] = $5 \mu\text{M}$; [ABDA] = $70 \mu\text{M}$.

thiophene bridge was adopted to connect the two acceptors. The synthetic route of **ADB** was shown in Scheme S1. Intermediate **A1** was prepared by the typical Pd-catalyzed Suzuki coupling reaction between 4,7-dibromo-2,1,3-benzothiadiazole and 4-(diphenylamino)phenylboronic acid. Then thiophene-2-carbaldehyde group was subsequently linked to **A1** to yield **A2** via the similar method. Finally, **ADB** was obtained through Knoevenagel condensation between **A2** and 2,3-dimethylbenzo[d]thiazol-3-ium iodide using pyridine as the catalyst. The detailed synthetic route, NMR and high-resolution mass spectra of **ADB** and the intermediates can be found in the Supplementary Material (Scheme S1, Figs. S1–S5).

UV–vis absorption and fluorescence spectrophotometer were used to investigate the optical properties of **ADB**. **ADB** had a good solubility in DMSO, CH₂Cl₂, CHCl₃ and other organic solvents. The absorption and emission peaks of **ADB** in different solvents were different (Fig. S6), and the values of which were summarized in Table S1. It was clear that **ADB** gave two absorption bands in the range of 300–340 nm and 470–580 nm in the solvents, which were derived from the π – π^* transition of the conjugated backbone structure and intramolecular charge transfer (ICT) between the D–A units [36,38,51–54], respectively. The ICT transition was further confirmed by the significantly solvent-dependent emission spectra as shown in Fig. S6b. The emission peak of **ADB** red-shifted obviously with the increasing of solvent polarity. For example, the maximum emission appeared at 659 nm in ethyl acetate, while it centered at 736 nm in DMSO, belonging to the near-infrared I region (Fig. 1d). In solid state, the emission maximum of **ADB** further red-shifted to 864 nm (Fig. 1e). Near-infrared emission has a large penetration depth, which can effectively avoid the interference of biological background fluorescence. At the same time, the Stokes shift of **ADB** in DMSO exceeded 200 nm, which could reduce the mutual interference between absorption and emission spectra, and improve the signal-to-noise ratio for biological imaging. The fluorescence lifetime of **ADB** solid powders and the cyclic voltammogram of **ADB** film were listed in Figs. S7 and S8, respectively. To investigate the AIE feature of **ADB**, its fluorescence spectra in toluene/DMSO mixture with different toluene fractions (f_t) were measured (Fig. 1f and Fig. S9). The fluorescence of **ADB** in DMSO was very weak because of the active intramolecular rotations in solution [55,56]. However, the fluorescence intensity of the mixture increased obviously with the increase of the ratio of toluene/DMSO. When the toluene fraction reached 95%, the fluorescence intensity was about 16 times higher than that in pure DMSO, revealing a typical AIE characteristics of **ADB**. The hydrodynamic diameter of **ADB** in water measured by dynamic light scattering (DLS) was in accordance with the result detected by TEM (Fig. S10), which confirmed the nanoparticle formation in aqueous solution. The absolute fluorescence quantum yields of **ADB** in DMSO solution ([**ADB**] = 10 μ M), aggregate ($f_t = 90\%$) and solid state were measured and the values were 6.9, 19.4 and 0.8% (excited at 500 nm), respectively. Comparing with other AIE-active fluorophores, **ADB** has bright emission in the near-infrared region [6,28,36]. The photostability of **ADB** was also analyzed. The fluorescence intensity of **ADB** only decreased by about 5.65% upon light (200 mW cm⁻²) irradiation for 10 min, and the absorption profile remained almost unchanged, indicating that **ADB** had a good photostability (Fig. S11).

3.2. ¹O₂ generation property of **ADB**

To evaluate the ¹O₂ generation efficiency of **ADB**, the classical dye 9,10-anthracenediyl-bis(methylene)dimalonic acid (ABDA) was used as an active oxygen indicator. As illustrated in Fig. 1g and h, the UV–vis absorption of ABDA solution without **ADB** remained almost unchanged after irradiation (400–700 nm, 50 mW cm⁻²) for 10 min. Whereas, in the presence of **ADB**, the absorption of ABDA solution at 378 nm decreased gradually with the increasing of irradiation time. After illumination for 270 s, the absorbance of ABDA decreased by 86.92%, which was almost difficult to detect. These results indicated that most ABDA was consumed by the ROS generated by **ADB**. Meanwhile, rose Bengal (RB) was selected as a reference. Under the same conditions, the absorption of ABDA at 378

nm only decreased by 49.65% after irradiation for 270 s (Fig. S12). Compared with RB, **ADB** could produce ROS more efficiently, and its ¹O₂ generation quantum yield was calculated to be 0.442 according to the method that have been reported previously [28,57,58]. These results proved that **ADB** could generate ROS effectively and could be used as a photosensitizer in photodynamic therapy.

Intersystem crossing from the lowest singlet excited state (S₁) to the lowest triplet excited state (T₁) plays a significant role in the generation of ¹O₂. To get a further insight into the molecular property of **ADB**, the theoretical calculation based on DFT/B3LYP/6-31G method was conducted. As could be seen in Fig. 1b, the lowest unoccupied molecular orbital (LUMO) of **ADB** was mainly distributed on the benzothiazole and thiophene units, while the highest occupied molecular orbital (HOMO) was mainly localized on the triphenylamine unit, which suggesting effective intramolecular charge transfer in **ADB**. The HOMO and LUMO were about –6.83 and –5.53 eV, respectively, and the energy gap of **ADB** was 1.30 eV. The relatively narrow band gap could result in red-shifted absorption and lower ΔE_{ST} , which was mainly attributed to the stronger electron push-pull effect in the D-A- π -A structure. The ΔE_{ST} value of **ADB** was calculated to be 0.6402 eV (Fig. 1c), indicating effective intersystem crossing from S₁ to T₁ state and highly efficient ¹O₂ generation [59–61].

3.3. Fluorescence imaging in vitro

The near-infrared emission, good photostability, large Stokes shift and efficient ¹O₂ generation of **ADB** encouraged us to further investigate its bioapplications. Biocompatibility was one of the deciding factors to determine whether the compound was suitable for the ensuing biological applications. So, the *in vitro* cytotoxicity of **ADB** towards HeLa, HepG2, MCF-7 and MCF-10 A cells was firstly measured by using the MTT method. As presented in Fig. 2, the cells could still retain >90% viability after incubation with 40 μ M **ADB** for 24 h, proving that **ADB** has low toxicity and good biocompatibility to cells, which opened the door for further biological applications.

To investigate its *in vitro* cellular imaging ability, **ADB** was incubated with MCF-7 cells for 6 h, and then observed with a confocal laser scanning microscope (CLSM). As shown in Fig. 3a, **ADB** could effectively accumulate in the cytoplasm and form a relatively uniform distribution around the nucleus, exhibiting bright red fluorescence signals. In addition, the fluorescence intensity in MCF-7 cells obviously enhanced with the increase of the concentration of **ADB** (Fig. 3b). This result proved that **ADB** could be internalized by cells and emitted red fluorescence in cells.

The two-photon imaging capability of **ADB** was further studied. The MCF-7 cells were incubated with **ADB** for 6 h and observed with a multi-photon laser scanning microscope. The excitation wavelength was adjusted in the range of 740–880 nm, and the fluorescence images were taken every 20 nm. It can be seen from Fig. 3c that the intracellular fluorescence gradually increased with the increase of excitation wavelength, and the intracellular fluorescence was the brightest when excited at 800 nm, then the fluorescence gradually faded, which was further confirmed by calculation of the average fluorescence intensity of the cells (Fig. 3d). The photostability of **ADB** upon continuous one-photon and two-photon laser excitation was also evaluated, as shown in Fig. S13, the intracellular fluorescence kept almost constant under laser irradiation for 9 min. These results indicated that **ADB** had excellent two-photon imaging potential and excellent photostability.

To examine the organelle targeting specificity of **ADB**, the fluorescence colocalization experiment was performed. MCF-7 cells were cocultured with **ADB** for 1, 2, 4 and 8 h, followed by incubation with Lyso-Tracker Green and Mito-Tracker Orange for 15 min respectively. Then the fluorescence distributions of these probes in the cells were observed with a CLSM. As shown in Fig. 3e, the NIR fluorescence of **ADB** almost completely overlapped with the green fluorescence of Lyso-Tracker Green, and the Pearson's correlation coefficients were 0.7639, 0.8596, 0.8778 and 0.8886 for lysosomes of MCF-7 cells cocultured with

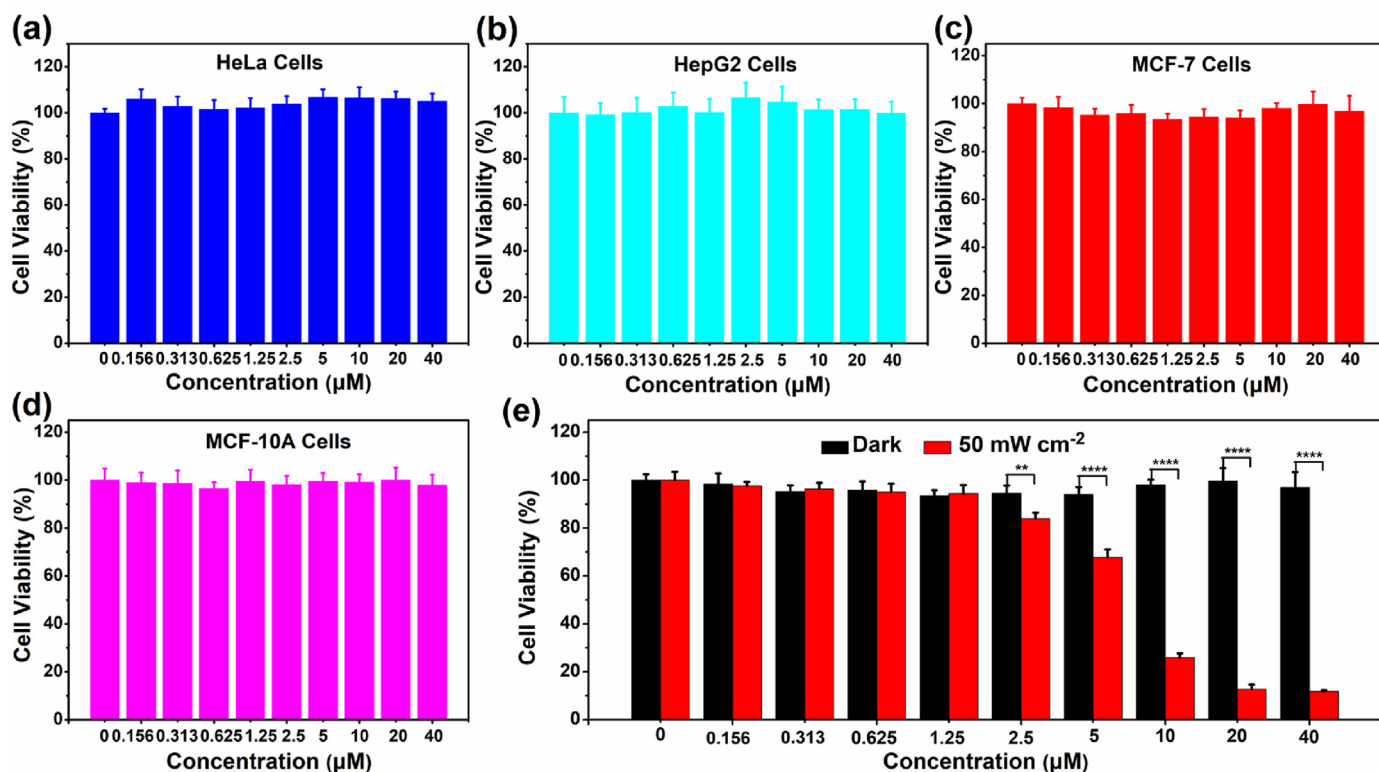


Fig. 2. Cell viability of (a) HeLa, (b) HepG2, (c) MCF-7 and (d) MCF-10 A cells treated with different concentrations of ADB using the MTT method. (e) Cell viability of MCF-7 cells incubated with ADB upon white light irradiation (400–700 nm, 50 mW cm^{-2}) for 10 min **, $P < 0.01$; ****, $P < 0.0001$.

ADB for 1, 2, 4 and 8 h respectively. At the same time, the fluorescence signals of Mito-Tracker Orange and ADB also overlapped fairly good with Pearson's coefficients of 0.4341, 0.6112, 0.7199 and 0.8139 for mitochondria of MCF-7 cells cocultured with ADB for 1, 2, 4 and 8 h respectively. It was noticed that the AIEgen ADB entered into lysosomes more rapidly than into mitochondria in the initial 2 h. Lysosomes were well known as the "waste disposal station" in the cell, so it was reasonable that they would capture ADB as extraneous particles rapidly when they entered cells. Meanwhile, the lipophilic and electrostatic interaction between ADB and mitochondria would facilitate the selective accumulation of ADB in the mitochondria, as confirmed by the Pearson's coefficients after 2 h. The details of the Quantitation analysis of the fluorescence intensities in MCF-7 cells were shown in Fig. S14 and were consistent with the cell imaging results. Fig. S15 further revealed the dual-specificity of ADB towards MCF-10 A normal cells after incubating for a period of time. These investigations distinctly demonstrated that ADB had high affinity for both lysosomes and mitochondria. This interesting mitochondria and lysosomes dual-organelles targeting capability would be very conducive to the photodynamic therapy of tumors.

3.4. In vitro PDT therapy using ADB

In the previous experiments, it was verified that ADB had bright NIR fluorescence, good biocompatibility, excellent bioimaging capability, specific dual-organelles targeting and high $^1\text{O}_2$ generation efficiency, which encouraged us to further explore its application potential in photodynamic therapy.

MTT method was used to detect the photodynamic effect of ADB on MCF-7 cells. As presented in Fig. 2e, after exposure to white light (400–700 nm, 50 mW cm^{-2}) for 10 min in the presence of 10 μM ADB, the survival rate of the cells was significantly reduced to 26.05%. When increasing the concentration of ADB to 20 μM , the survival rate of the cells was further reduced to 12.74%, and the IC_{50} value was 6.6 μM . As a

comparison, the cell viability of MCF-7 cells under dark remained above 90% at the same concentration of ADB. These results suggested that ADB has an excellent effect in photodynamic therapy.

In order to verify that ADB promotes cell apoptosis by producing $^1\text{O}_2$ in cells, 2,7-dichlorofluorescein diacetate (DCFH-DA) was utilized as an $^1\text{O}_2$ indicator. As shown in Fig. 4a, MCF-7 cells incubated with ADB exhibited bright green fluorescence after irradiation upon white light (400–700 nm, 50 mW cm^{-2}) for 10 min, confirming efficient generation of $^1\text{O}_2$. Whereas there was no discernible green fluorescence in ADB or light alone treated MCF-7 cells. It could be screened that ADB greatly enhanced the production of $^1\text{O}_2$ under irradiation, which may become an efficient photosensitizer for photodynamic therapy.

To further verify the PDT effect of ADB, a Calcein-AM/PI kit was used to detect live/dead cells. Fig. 4b showed that upon white light (400–700 nm, 50 mW cm^{-2}) irradiation for 10 min, MCF-7 cells cultured with ADB exhibited bright red fluorescence in the PI channel, while there was no green fluorescence could be observed in the AM channel, indicating that the cells were almost all dead. At the same time, for the cells treated by ADB or light alone, there was almost no red fluorescence in the PI channel whereas strong green fluorescence in the AM channel was observed, proving that the cells were still alive. These results further demonstrated that ADB had an outstanding PDT effect.

To further investigate the mechanism responsible for the organelle targeting-mediated PDT enhancement of ADB, the fluorescent probe JC-1 was adopted as an indicator to monitor the changes of mitochondrial membrane potential. As presented in Fig. 4c, for the cells without light irradiation, the green fluorescence was weak while the red fluorescence was relatively strong. However, upon light irradiation, the green fluorescence became stronger and the red fluorescence became weaker. The quantitation showed that there was a 2.6-fold increase in the intensity ratio of green-to-red (Fig. S16), indicating the decrease of MMP. Furthermore, biological transmission electron microscopy (bio-TEM) was conducted to observe the mitochondrial ultrastructure. As presented in

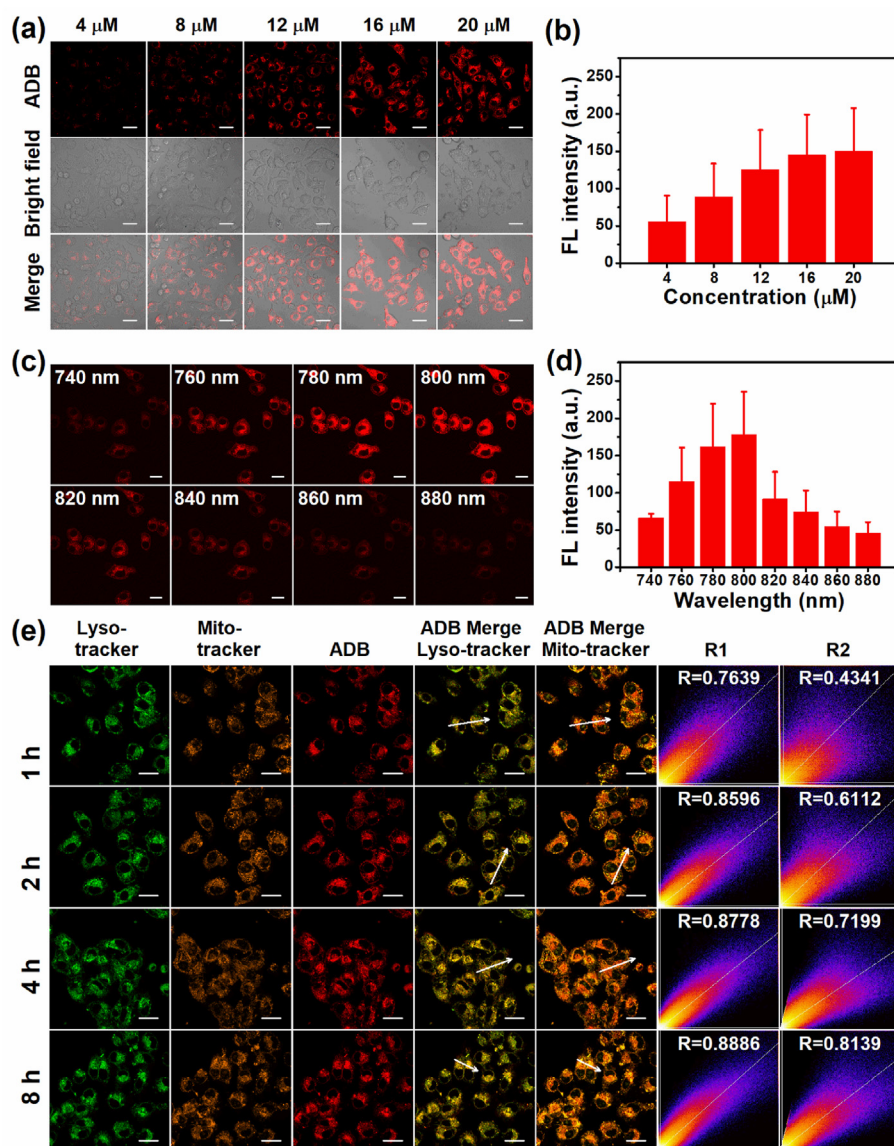


Fig. 3. (a) CLSM images of MCF-7 cells incubated with ADB at different concentrations for 6 h. Scale bars: 30 μm . (c) Two-photon fluorescence images of MCF-7 cells incubated with ADB (20 μM) upon excitation at different wavelengths. Scale bars: 20 μm . (b) and (d) Fluorescence intensities gathered from MCF-7 cells in (a) and (c) respectively. (e) CLSM images of MCF-7 cells incubated with ADB (20 μM) for 1, 2, 4 and 8 h, followed by co-staining with Lyso-Tracker Green and Mito-Tracker Orange, respectively. R1, Pearson's correlation coefficient of ADB merged with Lyso-Tracker Green; R2, Pearson's correlation coefficient of ADB merged with Mito-Tracker Orange. Scale bars: 20 μm .

Fig. 4e, without white light irradiation, the mitochondria with clear double membrane were well distributed in cytoplasm (green arrow). However, upon light irradiation, the mitochondria in MCF-7 cells treated with ADB showed obvious swollen, cavitation and crista fragmentation (purple arrow). Lysosome disruption analysis was undertaken by using Acridine Orange as indicator to monitor the integrity of the lysosomes. As presented in Fig. 4d, the red and green fluorescence in the PBS, PBS + light and ADB Groups meant that the lysosomes were intact, while in the ADB + light Group, the red fluorescence disappeared, indicating that the cell lysosomes were damaged by the $^1\text{O}_2$ burst. Furthermore, after careful observation of the bio-TEM images in Fig. 4e, it was amazing to find that there existed really some phagocytotic vesicles in the cells of the ADB + light Group, which were indicated by blue circles and arrows. There were obviously a number of nanoparticles in the phagocytotic vesicles, which providing direct evidence of the endocytosis of ADB nanoparticles by lysosomes, and perfectly indicating the lysosomes-targeting of ADB.

Taken together, these results clearly demonstrated the lysosomes and mitochondria dual-targeting of ADB nanoparticles, both of the critical organelles were damaged by the $^1\text{O}_2$ generated upon light irradiation, which further caused cell death and greatly enhanced the PDT effect.

3.5. Fluorescence imaging *in vivo*

Next, the use of ADB for *in vivo* fluorescence imaging of tumor-bearing mouse intratumorally injected with ADB (3 mg kg^{-1}) was performed, and the fluorescence signals at different post-injection time were recorded by a multispectral small animal imaging system. As could be seen from Fig. 5a, ADB was gradually absorbed by the tumor after injection, and the fluorescence intensified increasingly with time. After 3 h, ADB was diffused to the whole tumor, and the bright NIR fluorescence lightened the tumor site very clearly. Then the fluorescence intensity slightly weakened with a prolongation of time, but still remained at a relatively high level. The bright NIR fluorescence could still be seen at the tumor site after 72 h, proving that ADB had an effective tumor retention property. Quantification of the average fluorescence intensity of the images in Fig. 5a was shown in Fig. S17. After injection of ADB for 72 h, the mouse was sacrificed and the main organs and tumor were taken for *ex vivo* fluorescence imaging (Fig. 5b). The fluorescence signal could only be observed in the excised tumor and there was no NIR fluorescence in other organs. To further verify the metabolic capability of ADB, the *in vivo* fluorescence imaging was carried out again and the observation time was prolonged to 7 days. As shown in Fig. S18, the fluorescence intensity

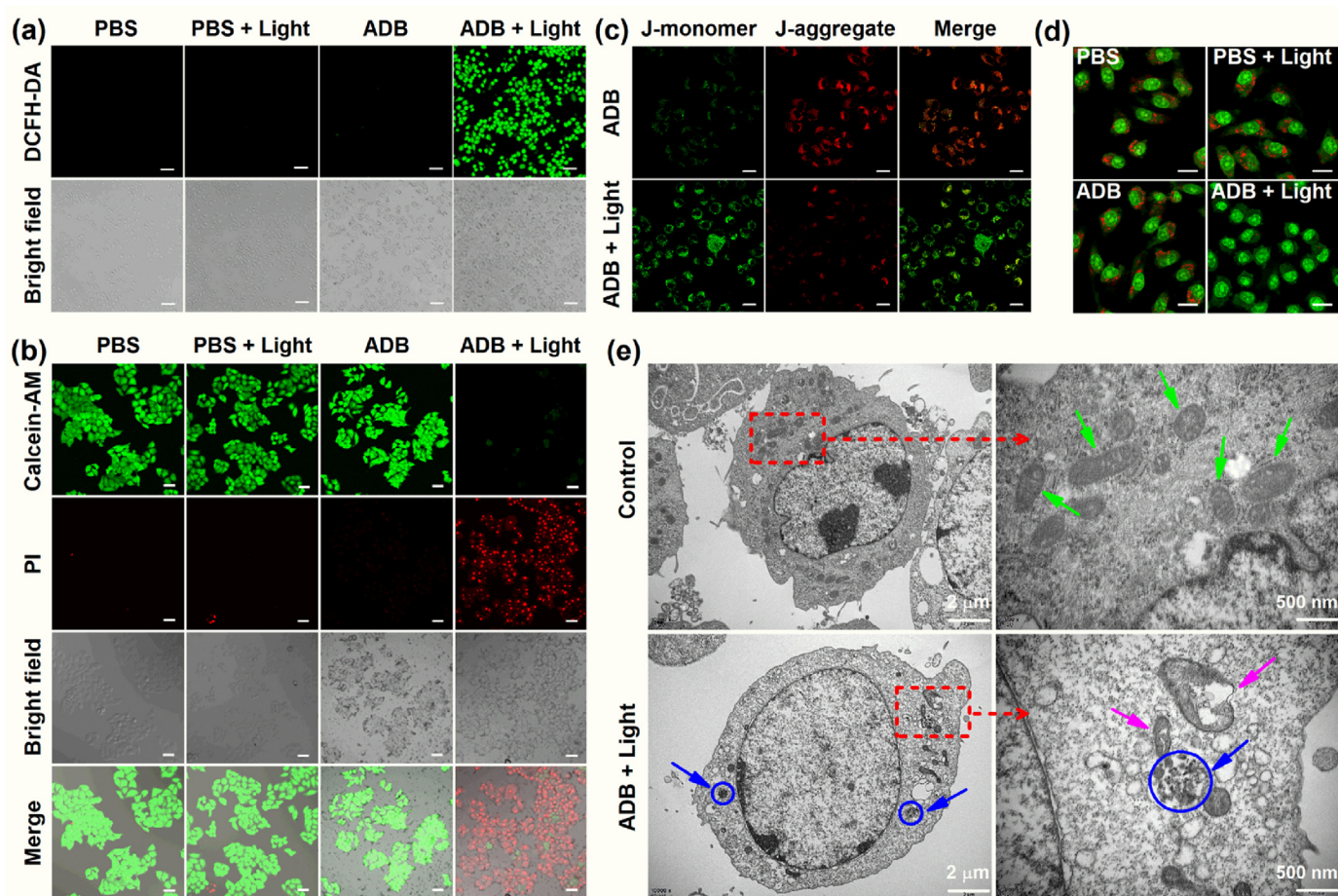


Fig. 4. (a) Confocal images of 1O_2 generation in MCF-7 cells stained with ADB (20 μ M) using DCFH-DA as an indicator upon white light irradiation (400–700 nm, 50 $mW\ cm^{-2}$). Scale bars: 100 μ m. (b) Confocal images of MCF-7 cells stained with ADB (20 μ M) using Calcein-AM/PI as the fluorescence probe upon irradiation (400–700 nm, 50 $mW\ cm^{-2}$). Scale bars: 50 μ m. (c) MMP analysis of MCF-7 cells using JC-1 mitochondrial membrane probe. Scale bars: 20 μ m. (d) Lysosome disruption analysis of MCF-7 cells after different treatments (green channel: λ_{ex} : 488 nm and λ_{em} : 500–540 nm; red channel: λ_{ex} : 561 nm and λ_{em} : 570–620 nm). Scale bars: 15 μ m. (e) The mitochondrial ultrastructure observed by bio-TEM.

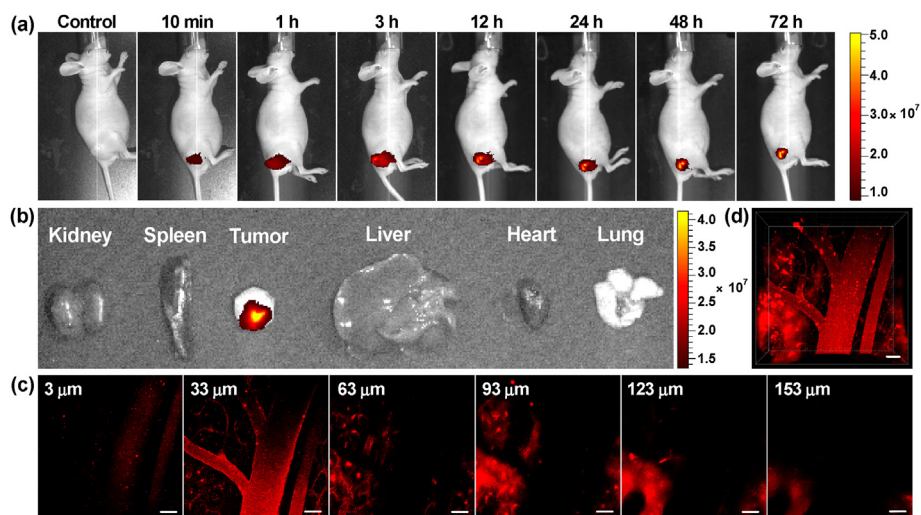


Fig. 5. (a) *In vivo* fluorescence imaging of tumor-bearing nude mice at different time points after intratumorally injected with ADB. (b) *Ex vivo* fluorescence images of the internal organs of mice after injection of ADB for 72 h. (c) Two-photon confocal images of mouse mesenteric vessels stained with ADB at a penetration depth from 3 to 153 μ m. (d) Reconstructed 3D image of mouse mesenteric vessels stained with ADB. Scale bars: 50 μ m, λ_{ex} : 800 nm.

obviously diminished after 96 h, and it was nearly disappeared after 7 days. These results proved that ADB could selectively accumulate at

tumor and retain in mouse body for an appropriate time, which would be very conducive to the following *in vivo* photodynamic therapy.

Considering the virtues of deeper penetration, high contrast and longer excitation wavelength of two-photon imaging, and simultaneously inspired by the excellent imaging capability of ADB in cells, *in vivo* two-photon tissue depth and time series fluorescence imaging of the mesenteric vessels of nude mouse was performed on a multi-photon laser scanning microscope. Because of its rich blood vessels and large blood flow, the mesenteric vessel was an ideal place for imaging. As shown in Fig. 5c and d, the mesenteric vessel network was clearly visualized and the imaging depth could reach 153 μm . Simultaneously, the time and 3D series vascular images in mesentery revealed that the blood flow could be dynamically observed (see SM videos). These results demonstrated that ADB had great potential in bioimaging and real-time tumor and organ monitoring.

3.6. ADB-mediated PDT therapy *in vivo*

The PDT performance of ADB *in vivo* was further investigated by establishing tumor-bearing mice model. The MCF-7 cells were subcutaneously inoculated to the lateral part of the right lower limb of the mouse. When the tumor volumes reached about 100 mm^3 , the mice were randomly divided into four groups for different treatments. Group 1: saline; Group 2: saline + light; Group 3: ADB and Group 4: ADB + light. After being subjected to different treatments, the body weights and tumor volumes of these mice were monitored (Fig. 6). It was noticed that the tumor volumes of the mice in Groups 1–3 gradually increased, and could reach about 8 times of magnitude to the initial volume after 14 days. In comparison, the tumor growth of the mice in Group 4 was effectively inhibited during the whole treatment period, and showing statistical difference to the control groups. The average tumor lengths,

widths and volumes of the mice in Groups 1–4 in different days were listed in Table S2 in the Supplementary Material. In addition, no significant difference in the body weight of the mice in Groups 1–4 was observed (Fig. S19). TUNEL analysis of tumor tissues (Fig. S20) further showed that there were large areas of apoptotic cells with condensed nuclei for the sample treated with ADB and white light irradiation (Group 4). These observations revealed that compound ADB could efficiently generate ROS upon irradiation and effectively suppress tumor growth, light exposure or ADB had no adverse effects on the growth of mice, which was further validated by the following pathological experiments.

H&E staining was carried out to assess the photoinduced damages to the main tissues and organs, and simultaneously evaluate the biocompatibility of ADB *in vivo*. As presented in Fig. 7, no obvious pathological abnormalities and damages were observed in the main organs (including heart, liver, spleen, lung and kidney) of the treated mice in Groups 1–4. However, it was noticed that in comparison with the other three groups, the H&E staining of the tumor slice after ADB + light treatment exhibited severe necrosis. The whole blood analyses revealed that there was no significant difference in the blood routine parameters (WBC (white blood cell), RBC (red blood cell), HGB (hemoglobin), HCT (hematocrit), MCV (mean corpuscular volume), MCH (mean corpuscular hemoglobin)) and hepatic and renal function markers (ALT (alanine aminotransferase), AST (aspartate aminotransferase), BUN (blood urea nitrogen) and CR (creatinine)) (Fig. S21). These results altogether demonstrated the great potential for ADB as an efficient photosensitizer for *in vivo* PDT, and confirmed the negligible toxicity and desirable biocompatibility of ADB, which were crucial for a photodynamic agent.

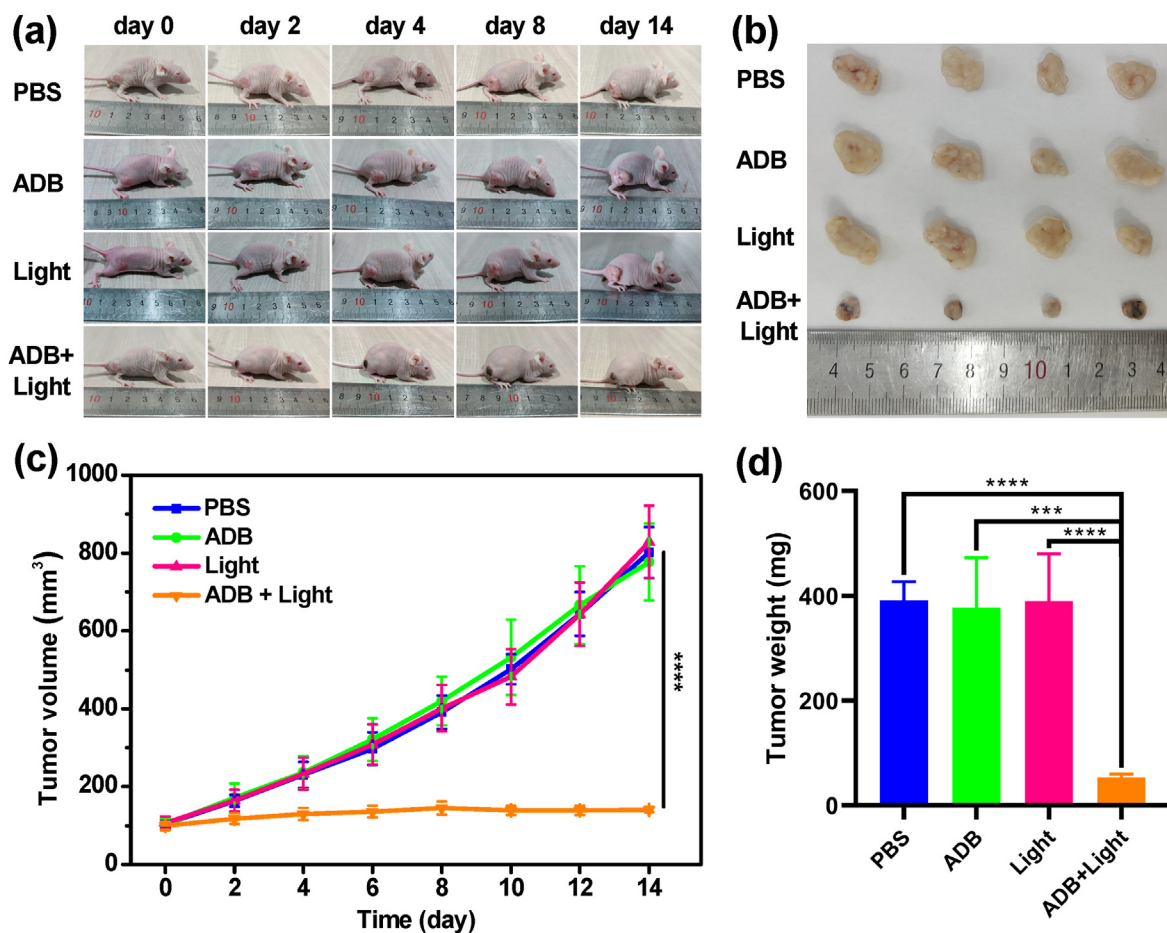


Fig. 6. (a) Photographs of living mice upon treatment for 14 days. (b) Photographs of tumors collected after different treatments. (c) Tumor growth curves of the mice during the process of different treatments. (d) Weights of dissected tumor after 14 days of treatments. ***, $P < 0.001$; ****, $P < 0.0001$.

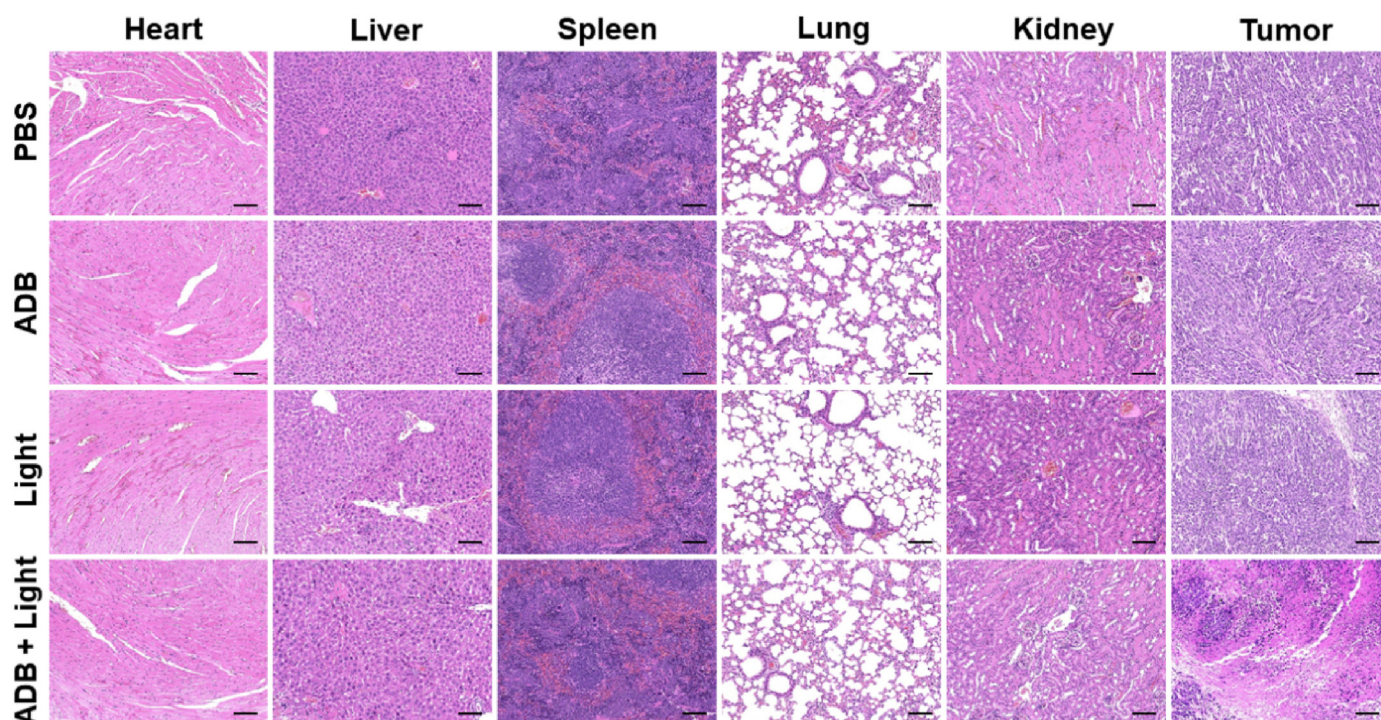


Fig. 7. H&E staining images of major organs of mice from Groups 1–4 subjected to different treatments. Scale bars: 100 μ m.

4. Conclusion

In summary, a lysosomes and mitochondria dual-organelles targeting organic photosensitizer, ADB, which possessed amphiphilic D-A- π -A structure, was rationally designed and synthesized. This positively charged AIE fluorophore exhibited good biocompatibility, high photostability, bright NIR emission and excellent two-photon bioimaging capability. *In vitro* investigations revealed that ADB nanoparticles could locate precisely at both lysosomes and mitochondria, and presented significant antitumor activity through efficient generation of reactive oxygen species which induced the damage of critical organelles upon light irradiation. More importantly, the imaging-guided *in vivo* PDT applied on MCF-7 tumor-bearing mice successfully suppressed tumor growth upon light exposure, demonstrating the great potential of using ADB for bioimaging and clinical imaging-guided photodynamic therapy applications. Moreover, this research provided a new sight for the design of multi-organelles targeted and more biocompatible NIR photosensitizers for phototheranostics.

Credit author statement

Shaozhen Wang: Conceptualization, Methodology, Investigation, Writing – original draft, Writing – review & editing. Yunhui Liao: Investigation, Methodology, Software. Zhaoji Wu: Investigation, Software. Yihong Peng: Investigation. Yuchen Liu: Investigation. Yinghua Chen: Methodology, Resources. Longquan Shao: Resources, Funding acquisition, Methodology, Validation, Writing – review. Zhijie Zeng: Project administration. Yanshan Liu: Conceptualization, Methodology, Resources, Funding acquisition, Project administration, Supervision, Writing – original draft, Writing – review & editing.

Declaration of competing interest

The authors declare that they have no known competing financial interests or personal relationships that could have appeared to influence the work reported in this paper.

Data availability

Data will be made available on request.

Acknowledgements

This work was financially supported by the Guangdong Natural Science Foundation (2018A030313976), the Open Fund of the State Key Laboratory of Luminescent Materials and Devices (South China University of Technology), China, 2022-skllmd-03, and National Natural Science Foundation of China (52072167). The authors are very grateful to Ting Guo and Lei Ying (South China University of Technology) for their selfless help during the experiment process.

Appendix A. Supplementary data

Supplementary data to this article can be found online at <https://doi.org/10.1016/j.mtbio.2023.100721>.

References

- [1] H. Sung, J. Ferlay, R.L. Siegel, M. Laversanne, I. Soerjomataram, A. Jemal, F. Bray, Global cancer statistics, GLOBOCAN estimates of incidence and mortality worldwide for 36 cancers in 185 countries, *Ca - Cancer J. Clin.* 71 (2021) 209–249.
- [2] X.S. Li, J.F. Lovell, J. Yoon, X.Y. Chen, Clinical development and potential of photothermal and photodynamic therapies for cancer, *Nat. Rev. Clin. Oncol.* 17 (2020) 657–673.
- [3] W.P. Fan, P. Huang, X.Y. Chen, Overcoming the achilles' heel of photodynamic therapy, *Chem. Soc. Rev.* 45 (2016) 6488–6519.
- [4] M.D. Yaqoob, L. Xu, C.F. Li, M.M.L. Leong, D.D. Xu, Targeting mitochondria for cancer photodynamic therapy, *Photodiagn. Photodyn.* 38 (2022) 102830.
- [5] M. Ethirajan, Y. Chen, P. Joshi, R.K. Pandey, The role of porphyrin chemistry in tumor imaging and photodynamic therapy, *Chem. Soc. Rev.* 40 (2011) 340–362.
- [6] W.B. Wu, D. Mao, S.D. Xu, M. Panahandeh-Fard, Y.K. Duan, F. Hu, D.L. Kong, B. Liu, Precise molecular engineering of photosensitizers with aggregation-induced emission over 800 nm for photodynamic therapy, *Adv. Funct. Mater.* 29 (2019) 1901791.
- [7] M.H. Lan, S.J. Zhao, W.M. Liu, C.S. Lee, W.J. Zhang, P.F. Wang, Photosensitizers for photodynamic therapy, *Adv. Healthcare Mater.* 8 (2019) 1900132.

- [8] R. Wang, X.S. Li, J. Yoon, Organelle-targeted photosensitizers for precision photodynamic therapy, *ACS Appl. Mater. Interfaces* 13 (2021) 19543–19571.
- [9] Z.J. Zhou, J.B. Song, L.M. Nie, X.Y. Chen, Reactive oxygen species generating systems meeting challenges of photodynamic cancer therapy, *Chem. Soc. Rev.* 45 (2016) 6597–6626.
- [10] C.K. Lim, J. Heo, S. Shin, K. Jeong, Y.H. Seo, W.D. Jang, C.R. Park, S.Y. Park, S. Kim, I.C. Kwon, Nanophotosensitizers toward advanced photodynamic therapy of cancer, *Cancer Lett.* 334 (2013) 176–187.
- [11] Y.J. Zhang, W.D. Huang, X.Y. Tan, J.H. Wang, Y.F. Zhao, J.B. Hu, S.H. Wang, A mitochondria-targeted dual-functional aggregation-induced emission luminogen for intracellular mitochondrial imaging and photodynamic therapy, *Biomater. Sci.* 9 (2021) 1232–1236.
- [12] J. Dai, X. Wu, S.Y. Ding, X.D. Lou, F. Xia, S.X. Wang, Y.N. Hong, Aggregation-induced emission photosensitizers: from molecular design to photodynamic therapy, *J. Med. Chem.* 63 (2020) 1996–2012.
- [13] J. Zhang, C.S. Jiang, J.P.F. Longo, R.B. Azevedo, H. Zhang, L.A. Muehlmann, An updated overview on the development of new photosensitizers for anticancer photodynamic therapy, *Acta Pharm. Sin.* 39 (2018) 137–146.
- [14] M. Gao, F.B. Yu, C.J. Lv, J. Choo, L.X. Chen, Fluorescent chemical probes for accurate tumor diagnosis and targeting therapy, *Chem. Soc. Rev.* 46 (2017) 2237–2271.
- [15] S. Hernot, L. van Manen, P. Debie, J.S.D. Mieog, A.L. Vahrmeijer, Latest developments in molecular tracers for fluorescence image-guided cancer surgery, *Lancet Oncol.* 20 (2019) e354–e367.
- [16] G.X. Feng, B. Liu, Aggregation-induced emission (AIE) dots: emerging theranostic nanolights, *Acc. Chem. Res.* 51 (2018) 1404–1414.
- [17] C.L. Zhu, R.T.K. Kwok, J.W.Y. Lam, B.Z. Tang, Aggregation-induced emission: a trailblazing journey to the field of biomedicine, *ACS Appl. Bio Mater.* 1 (2018) 1768–1786.
- [18] J.F. Lovell, T.W.B. Liu, J. Chen, G. Zheng, Activatable photosensitizers for imaging and therapy, *Chem. Rev.* 110 (2010) 2839–2857.
- [19] J.H. Correia, J.A. Rodrigues, S. Pimenta, T. Dong, Z.C. Yang, Photodynamic therapy review: principles, photosensitizers, applications, and future directions, *Pharmaceutics* 13 (2021) 1332.
- [20] X.Z. Zhao, J.P. Liu, J.L. Fan, H. Chao, X.J. Peng, Recent progress in photosensitizers for overcoming the challenges of photodynamic therapy: from molecular design to application, *Chem. Soc. Rev.* 50 (2021) 4185–4219.
- [21] Z.J. Wang, L. Yu, Y.H. Wang, C.L. Wang, Q.C. Mu, X.J. Liu, M. Yu, K.-N. Wang, G.Y. Yao, Z.Q. Yu, Dynamic adjust of non-radiative and radiative attenuation of AIE molecules reinforces NIR-II imaging mediated photothermal therapy and immunotherapy, *Adv. Sci.* 9 (2022) 2104793.
- [22] G.L. Niu, R.Y. Zhang, Y. Gu, J.G. Wang, C. Ma, R.T.K. Kwok, J.W.Y. Lam, H.H.Y. Sung, I.D. Williams, K.S. Wong, X.Q. Yu, B.Z. Tang, Highly photostable two-photon NIR AIEgens with tunable organelle specificity and deep tissue penetration, *Biomaterials* 208 (2019) 72–82.
- [23] J. Luo, Z. Xie, J.W.Y. Lam, L. Cheng, H. Chen, C. Qiu, H.S. Kwok, X. Zhan, Y. Liu, D. Zhu, B.Z. Tang, Aggregation-induced emission of 1-methyl-1,2,3,4,5-pentaphenylsilole, *Chem. Commun.* 18 (2001) 1740–1741.
- [24] Y.N. Hong, J.W.Y. Lam, B.Z. Tang, Aggregation-induced emission, *Chem. Soc. Rev.* 40 (2011) 5361–5388.
- [25] Y.C. Chen, J.W.Y. Lam, R.T.K. Kwok, B. Liu, B.Z. Tang, Aggregation-induced emission: fundamental understanding and future developments, *Mater. Horiz.* 6 (2019) 428–433.
- [26] X.L. Cai, B. Liu, Aggregation-induced emission: recent advances in materials and biomedical applications, *Angew. Chem. Int. Ed.* 59 (2020), 9868–9886.
- [27] Y.Y. Lai, J.L. Huang, S.G. Wu, Q.H. Zhu, Y.S. Liu, Aggregation-induced emission and reversible mechanofluorochromic characteristics of tetra-substituted tetrahydropyrimidine derivatives, *Dyes Pigments* 166 (2019) 8–14.
- [28] Y.H. Liao, R.L. Wang, S.Z. Wang, Y.F. Xie, H.H. Chen, R.J. Huang, L.Q. Shao, Q.H. Zhu, Y.S. Liu, Highly efficient multifunctional organic photosensitizer with aggregation-induced emission for *in vivo* bioimaging and photodynamic therapy, *ACS Appl. Mater. Interfaces* 13 (2021) 54783–54793.
- [29] Y.Y. Yuan, G.X. Feng, W. Qin, B.Z. Tang, B. Liu, Targeted and image-guided photodynamic cancer therapy based on organic nanoparticles with aggregation-induced emission characteristics, *Chem. Commun.* 50 (2014), 8757–8760.
- [30] X.G. Gu, R.T.K. Kwok, J.W.Y. Lam, B.Z. Tang, AIEgens for biological process monitoring and disease theranostics, *Biomaterials* 146 (2017) 115–135.
- [31] D.Y. Yan, M. Wang, Q. Wu, N. Niu, M. Li, R.X. Song, J. Rao, M.M. Kang, Z.J. Zhang, F.F. Zhou, D. Wang, B.Z. Tang, Multimodal imaging-guided photothermal immunotherapy based on a versatile NIR-II aggregation-induced emission luminogen, *Angew. Chem. Int. Ed.* 61 (2022) e202202614.
- [32] M. Yang, Z. Zeng, J.W.Y. Lam, J. Fan, K. Pu, B.Z. Tang, State-of-the-art self-luminescence: a win-win situation, *Chem. Soc. Rev.* 51 (2022) 8815–8831.
- [33] H. Zou, J. Zhang, C. Wu, B. He, Y. Hu, H.H.Y. Sung, R.T.K. Kwok, J.W.Y. Lam, L. Zheng, B.Z. Tang, Making aggregation-induced emission luminogen more valuable by gold: enhancing anticancer efficacy by suppressing thioredoxin reductase activity, *ACS Nano* 15 (2021) 9176–9185.
- [34] S. Liu, G. Feng, B.Z. Tang, B. Liu, Recent advances of AIE light-up probes for photodynamic therapy, *Chem. Sci.* 12 (2021) 6488–6506.
- [35] G.R. Jin, G.X. Feng, W. Qin, B.Z. Tang, B. Liu, K. Li, Multifunctional organic nanoparticles with aggregation-induced emission (AIE) characteristics for targeted photodynamic therapy and RNA interference therapy, *Chem. Commun.* 52 (2016) 2752–2755.
- [36] L.P. Zhang, W.L. Che, Z.Y. Yang, X.M. Liu, S. Liu, Z.G. Xie, D.X. Zhu, Z.M. Su, B.Z. Tang, M.R. Bryce, Bright red aggregation-induced emission nanoparticles for multifunctional applications in cancer therapy, *Chem. Sci.* 11 (2020) 2369–2374.
- [37] W.H. Zhuang, L. Yang, B.X. Ma, Q.S. Kong, G.C. Li, Y.B. Wang, B.Z. Tang, Multifunctional two-photon AIE luminogens for highly mitochondria-specific bioimaging and efficient photodynamic therapy, *ACS Appl. Mater. Interfaces* 11 (2019) 20715–20724.
- [38] Z.Y. He, Y.T. Gao, H.M. Zhang, Y. Xue, F.L. Meng, L. Luo, Mitochondrion-anchored photosensitizer with near infrared-I aggregation-induced emission for near infrared-II two-photon photodynamic therapy, *Adv. Healthcare Mater.* 10 (2021) 2101056.
- [39] Y.P. Zhou, D. Zhang, G.H. He, C. Liu, Y.N. Tu, X. Li, Q.B. Zhang, X. Wu, R.Y. Liu, A lysosomal targeted NIR photosensitizer for photodynamic therapy and two-photon fluorescence imaging, *J. Mater. Chem. B* 9 (2021) 1009–1017.
- [40] B. Gu, W.B. Wu, G.X. Xu, G.X. Feng, F. Yin, P.H.J. Chong, J.L. Qu, K.-T. Yong, B. Liu, Precise two-photon photodynamic therapy using an efficient photosensitizer with aggregation-induced emission characteristics, *Adv. Mater.* 29 (2017) 1701076.
- [41] S. Kim, T. Tachikawa, M. Fujitsuka, T. Majima, Far-red fluorescence probe for monitoring singlet oxygen during photodynamic therapy, *J. Am. Chem. Soc.* 136 (2014) 11707–11715.
- [42] G.X. Feng, W. Qin, Q.L. Hu, B.Z. Tang, B. Liu, Cellular and mitochondrial dual-targeted organic dots with aggregation-induced emission characteristics for image-guided photodynamic therapy, *Adv. Healthcare Mater.* 4 (2015) 2667–2676.
- [43] Y.Y. Huang, G.X. Zhang, R. Zhao, D.Q. Zhang, Aggregation-induced emission luminogens for mitochondria-targeted cancer therapy, *ChemMedChem* 15 (2020) 2220–2227.
- [44] H. Appelqvist, P. Waster, K. Kagedal, K. Ollinger, The lysosome: from waste bag to potential therapeutic target, *J. Mol. Cell Biol.* 5 (2013) 214–226.
- [45] J. Yang, A. Griffin, Z. Qiang, J. Ren, Organelle-targeted therapies: a comprehensive review on system design for enabling precision oncology, *Signal Transduct. Targeted Ther.* 7 (2022) 379.
- [46] T.F. Zhang, J.Y. Zhang, F.B. Wang, H. Cao, D.M. Zhu, X.Y. Chen, C.H. Xu, X.Q. Yang, W.B. Huang, Z.Y. Wang, J.F. Wang, Z.K. He, Z. Zheng, J.W. Y. Lam, B.Z. Tang, Mitochondria-targeting phototheranostics by aggregation-induced NIR-II emission luminogens: modulating intramolecular motion by electron acceptor engineering for multi-modal synergistic therapy, *Adv. Funct. Mater.* 32 (2022) 2110526.
- [47] H.D. Li, Y. Lu, J. Chung, J.J. Han, H. Kim, Q.C. Yao, G. Kim, X.F. Wu, S.R. Long, X.J. Peng, J.Y. Yoon, Activation of apoptosis by rationally constructing NIR amphiphilic AIEgens: surmounting the shackle of mitochondrial membrane potential for amplified tumor ablation, *Chem. Sci.* 12 (2021) 10522–10531.
- [48] X.H. Chen, Y.X. Li, S.W. Li, M. Gao, L. Ren, B.Z. Tang, Mitochondria- and lysosomes-targeted synergistic chemo-photodynamic therapy associated with self-monitoring by dual light-up fluorescence, *Adv. Funct. Mater.* 28 (2018) 1804362.
- [49] C.X. Chai, T. Zhou, J.F. Zhu, Y. Tang, J. Xiong, X.B. Min, Q. Qin, M. Li, N. Zhao, C.D. Wan, Multiple light-activated photodynamic therapy of tetraphenylethylene derivative with AIE characteristics for hepatocellular carcinoma via dual-organelles targeting, *Pharmaceutics* 14 (2022) 459.
- [50] D.H. Wang, L.J. Chen, X. Zhao, X.P. Yan, Rational design of a dual organelle-targeted photosensitizer with dual-color emission for photodynamic therapy and cell death self-reporting, *Dyes Pigments* 203 (2022) 110315.
- [51] P. Galer, R.C. Korošec, M. Vidmar, B. Šket, Crystal structures and emission properties of the BF₂ complex 1-phenyl-3-(3,5-dimethoxyphenyl)propane-1,3-dione: multiple chromisms, aggregation- or crystallization-induced emission, and the self-assembly effect, *J. Am. Chem. Soc.* 136 (2014) 7383–7394.
- [52] F.L. Guo, Z.Q. Li, X.P. Liu, L. Zhou, F.T. Kong, W.C. Chen, S.Y. Dai, Metal-free sensitizers containing hydantoin acceptor as high performance anchoring group for dye-sensitized solar cells, *Adv. Funct. Mater.* 26 (2016) 5733–5740.
- [53] Z.Q. Zhang, Z. Wu, J.B. Sun, B.Q. Yao, P.C. Xue, R. Lu, β -Iminoenolate boron complex with terminal triphenylamine exhibiting polymorphism and mechanofluorochromism, *J. Mater. Chem. C* 4 (2016) 2854–2861.
- [54] M. Chen, H. Nie, B. Song, L.Z. Li, J.Z. Sun, A.J. Qin, B.Z. Tang, Triphenylamine-functionalized tetraphenylpyrazine: facile preparation and multifaceted functionalities, *J. Mater. Chem. C* 4 (2016) 2901–2908.
- [55] K.Q. Chen, P. He, Z.M. Wang, B.Z. Tang, A feasible strategy of fabricating type I photosensitizer for photodynamic therapy in cancer cells and pathogens, *ACS Nano* 15 (2021) 7735–7743.
- [56] J. Mei, Y.N. Hong, J.W.Y. Lam, A.J. Qin, Y.H. Tang, B.Z. Tang, Aggregation-induced emission: the whole is more brilliant than the parts, *Adv. Mater.* 26 (2014) 5429–5479.
- [57] J.L. Zou, H.G. Lu, X.W. Zhao, W. Li, Y. Guan, Y.D. Zheng, L.J. Zhang, H. Gao, A multi-functional fluorescent probe with aggregation-induced emission characteristics: mitochondrial imaging, photodynamic therapy and visualizing therapeutic process in zebrafish model, *Dyes Pigments* 151 (2018) 45–53.
- [58] S.D. Xu, Y.Y. Yuan, X.L. Cai, C.J. Zhang, F. Hu, J. Liang, G.X. Zhang, D.Q. Zhang, B. Liu, Tuning the singlet-triplet energy gap: a unique approach to efficient photosensitizers with aggregation-induced emission (AIE) characteristics, *Chem. Sci.* 6 (2015) 5824–5830.
- [59] H.J. Ma, C. Zhao, H.B. Meng, R.X. Li, L.C. Mao, D.N. Hu, M. Tian, J.Y. Yuan, Y. Wei, Multifunctional organic fluorescent probe with aggregation-induced emission characteristics: ultrafast tumor monitoring, two-photon imaging, and image-guide photodynamic therapy, *ACS Appl. Mater. Interfaces* 13 (2021) 7987–7996.
- [60] X.G. Gu, X.Y. Zhang, H.L. Ma, S.R. Jia, P.F. Zhang, Y.J. Zhao, Q. Liu, J.G. Wang, X.Y. Zheng, J.W.Y. Lam, D. Ding, B.Z. Tang, Corannulene-incorporated AIE nanodots with highly suppressed nonradiative decay for boosted cancer phototheranostics *in vivo*, *Adv. Mater.* 30 (2018) 1801065.
- [61] X.F. Miao, W.B. Hu, T.C. He, H.J. Tao, Q. Wang, R.F. Chen, L. Jin, H. Zhao, X.M. Lu, Q.L. Fan, W. Huang, Deciphering the intersystem crossing in near-infrared BODIPY photosensitizers for highly efficient photodynamic therapy, *Chem. Sci.* 10 (2019) 3096–3102.